Stimuli-responsive lipid-based magnetic nanovectors increase apoptosis in glioblastoma cells through synergic intracellular hyperthermia and chemotherapy

Volume 11 | Number 1 | 7 January 2019 | Pages 1–368

Nanoscale

rsc.li/nanoscale

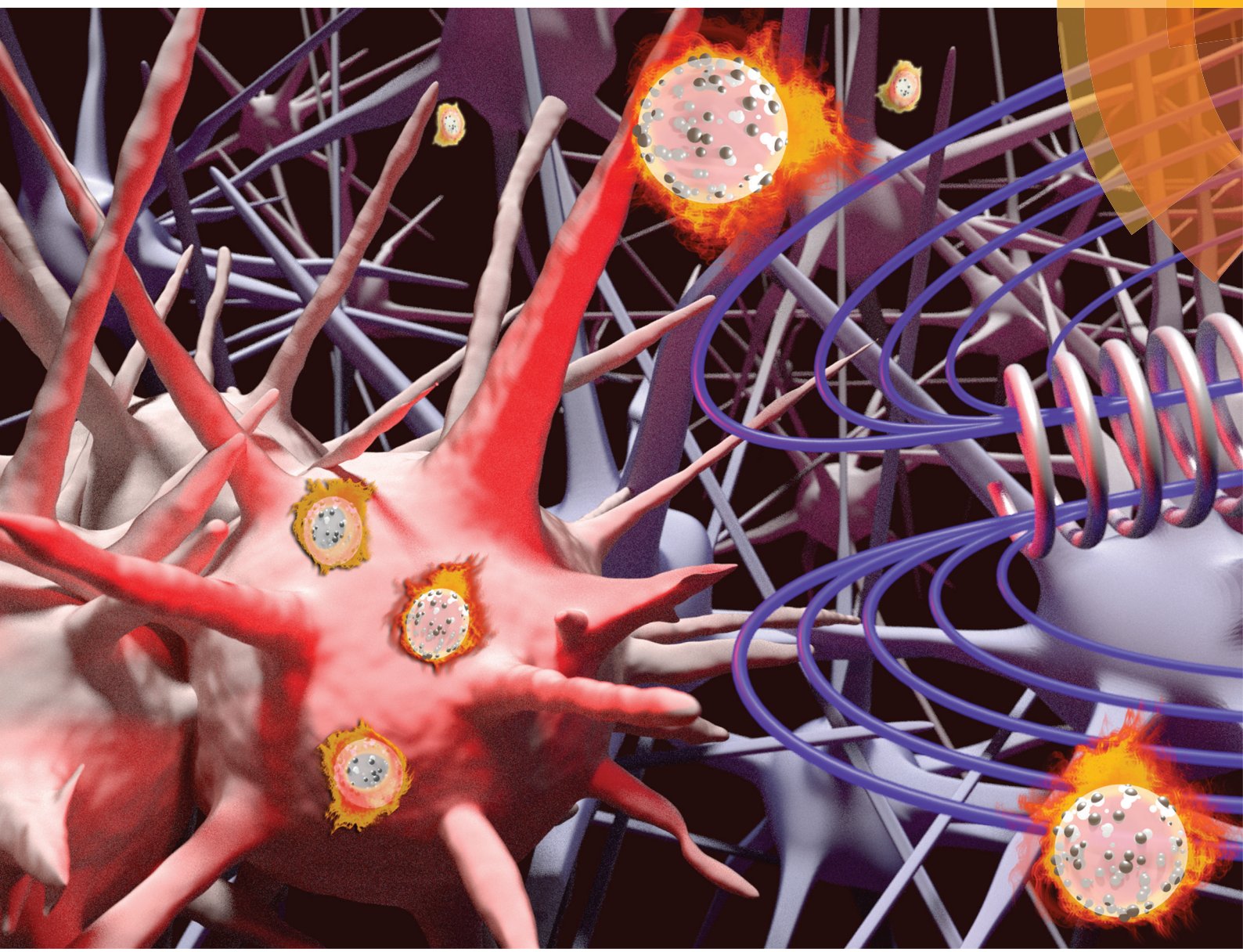

ISSN 2040-3372

ROYAL SOCIETY OF CHEMISTRY | Celebrating IYPT 2019

PAPER

Christos Tapeinos, Attilio Marino, Gianni Ciofani *et al.*
Stimuli-responsive lipid-based magnetic nanovectors increase apoptosis in glioblastoma cells through synergic intracellular hyperthermia and chemotherapy

NCNST

Nanoscale

PAPER

View Article Online
View Journal | View Issue

Cite this: *Nanoscale*, 2019, **11**, 72

Stimuli-responsive lipid-based magnetic nanovectors increase apoptosis in glioblastoma cells through synergic intracellular hyperthermia and chemotherapy†

Christos Tapeinos, *‡[a] Attilio Marino,*‡[a] Matteo Battaglini,[a,b] Simone Migliorin,[c] Rosaria Brescia,[d] Alice Scarpellini,[d] César De Julián Fernández,[e] Mirko Prato,[f] Filippo Drago[g] and Gianni Ciofani *[a,c]

In this study, taking into consideration the limitations of current treatments of glioblastoma multiforme, we fabricated a biomimetic lipid-based magnetic nanovector with a good loading capacity and a sustained release profile of the encapsulated chemotherapeutic drug, temozolomide. These nanostructures demonstrated an enhanced release after exposure to an alternating magnetic field, and a complete release of the encapsulated drug after the synergic effect of low pH (4.5), increased concentration of hydrogen peroxide (50 μM), and increased temperature due to the applied magnetic field. In addition, these nanovectors presented excellent specific absorption rate values (up to 1345 W g^{-1}) considering the size of the magnetic component, rendering them suitable as potential hyperthermia agents. The presented nanovectors were progressively internalized in U-87 MG cells and in their acidic compartments (*i.e.*, lysosomes and late endosomes) without affecting the viability of the cells, and their ability to cross the blood–brain barrier was preliminarily investigated using an *in vitro* brain endothelial cell-model. When stimulated with alternating magnetic fields (20 mT, 750 kHz), the nanovectors demonstrated their ability to induce mild hyperthermia (43 °C) and strong anticancer effects against U-87 MG cells (scarce survival of cells characterized by low proliferation rates and high apoptosis levels). The optimal anticancer effects resulted from the synergic combination of hyperthermia chronic stimulation and the controlled temozolomide release, highlighting the potential of the proposed drug-loaded lipid magnetic nanovectors for treatment of glioblastoma multiforme.

Received 9th July 2018,
Accepted 1st October 2018

DOI: 10.1039/c8nr05520c

rsc.li/nanoscale

Introduction

Glioblastoma multiforme (GBM) is one of the most malignant brain tumors associated with high percentages of mortality worldwide and with a 5-year survival rate of less than 10%.[1]

The reason for the inability to treat this form of cancer lies in several factors, including its rapid growth, the location and the pathophysiology of the tumor that in many cases forbid its surgical resection, and the blood–brain barrier (BBB) that hinders efficient delivery of various chemotherapeutics to the malignant tissue.[1–3]

The contemporary approaches for the treatment of GBM consist of surgical resection, radiotherapy (the role of which is controversial), adjuvant or neoadjuvant chemotherapy using temozolomide, and, finally, hyperthermia using superparamagnetic iron oxide nanoparticles.[4,5] Although in certain cases the median overall survival of patients increases, in the majority of the patients these treatments have a more palliative than curative role.

The combination of surgical resection and chemotherapy is used as a gold standard for many forms of cancer (*e.g.*, breast, prostate, pancreatic, *etc.*), but, unfortunately, not all patients are able to undergo this combinatory therapy, leading to an unmet clinical need. In addition, in many cases where the

[a]*Smart Bio-Interfaces, Istituto Italiano di Tecnologia, Pontedera (Pisa), 56025 Italy. E-mail: christos.tapeinos@iit.it, attilio.marino@iit.it, gianni.ciofani@iit.it*
[b]*The Biorobotics Institute, Scuola Superiore Sant'Anna, Pontedera (Pisa), 56025 Italy*
[c]*Department of Mechanical and Aerospace Engineering, Politecnico di Torino, Torino, 10129 Italy*
[d]*Electron Microscopy Facility, Istituto Italiano di Tecnologia, Genova, 16163 Italy*
[e]*Istituto dei Materiali per l'Elettronica e il Magnetismo, Consiglio Nazionale delle Ricerche – CNR, Parma, 43124 Italy*
[f]*Materials Characterization Facility, Istituto Italiano di Tecnologia, Genova, 16163 Italy*
[g]*Nanochemistry Department, Istituto Italiano di Tecnologia, Genova, 16163 Italy*
†Electronic supplementary information (ESI) available. See DOI: 10.1039/c8nr05520c
‡These authors contributed equally to this work.

patient can undergo this combinatory treatment, the side-effects of the administered chemotherapeutics negatively affect the quality of life of the patient, resulting in a controversy concerning their use. Radiotherapy is another form of treatment which is also used in combination with chemotherapy, in cases where surgery cannot be performed, but this combination is not only less effective than chemotherapy and surgery, but also results in an increased number of side effects, causing the same controversies as chemotherapy.

One of the reasons for the low success rates in increasing patient survival stems from the low efficacy of the used chemotherapeutics due to various causes, including the fast reticuloendothelial system clearance, the non-controllable biodistribution, and the inability to cross the BBB.[1,6,7]

In order to overcome the limitations that the current chemotherapeutics like temozolomide (TMZ) present, these chemical substances are encapsulated inside delivery vehicles aiming at improving their efficacy. These delivery vehicles are made of a variety of different materials like synthetic and/or natural polymers and lipids, and can be in the form of microspheres, nanospheres, nanoparticles, micelles, nanorods, nanotubes, hydrogels, and others.[8–12] Each one of these systems presents its own advantages and disadvantages and depending on the application, a different type is used every time.

These vectors can be also designed in a way to alter their physicochemical properties under a specific stimulus, which can be either physical, chemical, biological, or any combination of them. This ability enhances the efficacy of the synthesized vehicles, since, by controlling their properties, drug release, increase of temperature, or their guidance in the cancerous tissue can be achieved in a controlled manner.[8,11,13]

These delivery vehicles (or nanovectors) demonstrate a biomimetic character with increased biocompatibility and low immunogenicity, which allows them, as mentioned above, to effectively deliver in a controlled way various therapeutic substances. Their small size and their ability to be coated with a variety of natural or synthetic materials allow them to increase their circulation time in the blood, and to effectively deliver the encapsulated therapeutic molecules towards the tissue of interest. Because of the difficulty that the majority of the used therapeutic agents face in crossing the BBB, a limited number of nanovectors can be used for the treatment of GBM and these nanovectors are composed of various lipids that can be classified into different types, the most common of which include solid lipid nanoparticles (SLNs), nanostructured lipid carriers (NLCs), and liposomes (LS).[14] These nanovectors present an inherent ability to cross the BBB and when properly functionalized demonstrate an enhanced targeting ability and a subsequent increased uptake by the endothelial cells of the BBB, as well as by glioblastoma cells like the U-87 and U-251 malignant glioma (MG) cells.

During the last few years, and especially after the Food and Drug Administration (FDA) approved the use of superparamagnetic iron oxide nanoparticles (SPIONs) as magnetic resonance imaging contrast agents as well as for the treatment of brain cancer using hyperthermia, many researchers have presented studies where lipid-based delivery vehicles encapsulating magnetite nanoparticles (Fe_3O_4) and/or chemotherapeutic agents were used for the treatment of this and other types of cancer.[11,15–17]

During hyperthermia, inorganic nanoparticles like magnetite or maghemite (γ-Fe_2O_3), coated with synthetic materials like polymers or with natural-derived materials like collagen, albumin, lipids and others, are subjected to an alternating magnetic field (AMF) of a specific frequency, which forces them to increase the temperature of their surrounding environment due to dissipative losses (Néelian, Brownian, and hysteresis).[18]

It should be noted that, although magnetic hyperthermia is not a novel concept for the treatment of various types of cancer, to date its use has been either experimental or it has been restricted only to patients in a small number of clinical trials, and this is mainly because the use of hyperthermia alone is not enough to cure GBM.

Taking into consideration all the above limitations concerning the use of smart drug delivery systems, we hypothesized that the combination of magnetic hyperthermia, using SPIONs encapsulated in a lipid-based nanovector, and the sustained release of TMZ, a golden standard for GBM, will increase the therapeutic efficacy of the designed nanovector, resulting into increased apoptosis and in the subsequent death of glioblastoma cells. A simple one-pot procedure was used to synthesize the composite nanovectors, which were morphologically, physicochemically, and magnetically characterized. The designed lipid-based magnetic nanovectors (LMNVs) demonstrated high stability in water as well as in media that simulated the body fluids and a sustained release profile for a period of seven days. The LMNVs succeeded in increasing the temperature of the solution from 37 °C to 43 °C in just a few minutes with better hyperthermia properties (specific absorption rate and intrinsic loss power) than bare SPIONs. Chronic stimulation under an AMF of the U-87 MG cell line, in the presence of just 400 μg cm^{-2} of LMNVs, led to an increase in apoptosis after 4 days by 50%, and to a reduction of proliferation by 80%.

Results and discussion

Synthesis procedure

The lipid-based magnetic nanovectors used in this study were fabricated following a combination of the hot ultra-sonication and high pressure homogenization (HPH) methods. Ultra-sonication resulted in the formation of a nano-emulsion which was further homogenized using the HPH. Dynamic light scattering studies on LMNVs fabricated only by the hot ultra-sonication method (results not presented here) demonstrated that the nanovectors had a similar hydrodynamic diameter but increased polydispersity, rendering mandatory the use of HPH in order to achieve a monodisperse population. The temperature for the melting and subsequent homogenization of the lipid mixture was chosen to be 70 °C, which is higher than the melting temperature (57–65 °C) of the primary lipid (glycerol

monostearate, GMS), in order to have a homogeneous dispersion of the secondary lipids as well as of the SPIONs in the main lipid matrix. In addition, this temperature is close to the boiling point of ethanol, which is used as a dispersant for the SPIONs, allowing its complete evaporation and the formation of a homogeneous liquid film. The choice of Tween® 80 as a stabilizer was made based on the literature findings where it is demonstrated that Tween® 80 enhances the delivery of nanoparticles across the BBB due to its ability to adsorb a variety of lipoproteins such as apo-lipoprotein A, E, and others.[19,20]

Morphological and physicochemical characterization

The LMNVs were firstly characterized using transmission electron microscopy (TEM) and the results are presented in Fig. 1A (and in ESI, Fig. S1†). The LMNVs present a spherical shape and a relatively low polydispersity in the nanometer range. Their size distribution after analysis with ImageJ (see ESI, Fig. S1C†) shows that 86% of the nanovectors have a size of less than 50 nm with only a small number of them exceeding 100 nm. These results are in agreement with dynamic light scattering as well as with nanoparticle tracking analysis (NTA) data that are presented below. The magnified image of the unstained LMNV presented in Fig. 1A2 demonstrates the homogeneous dispersion of the SPIONs inside the lipid matrix of the nanovectors, which was also proved by the electron dispersive X-ray (EDS) mapping of iron (Fe) and oxygen (O) in Fig. 1A3 and A4, respectively. In order to quantify the amount of each element in the fabricated LMNVs, we performed an

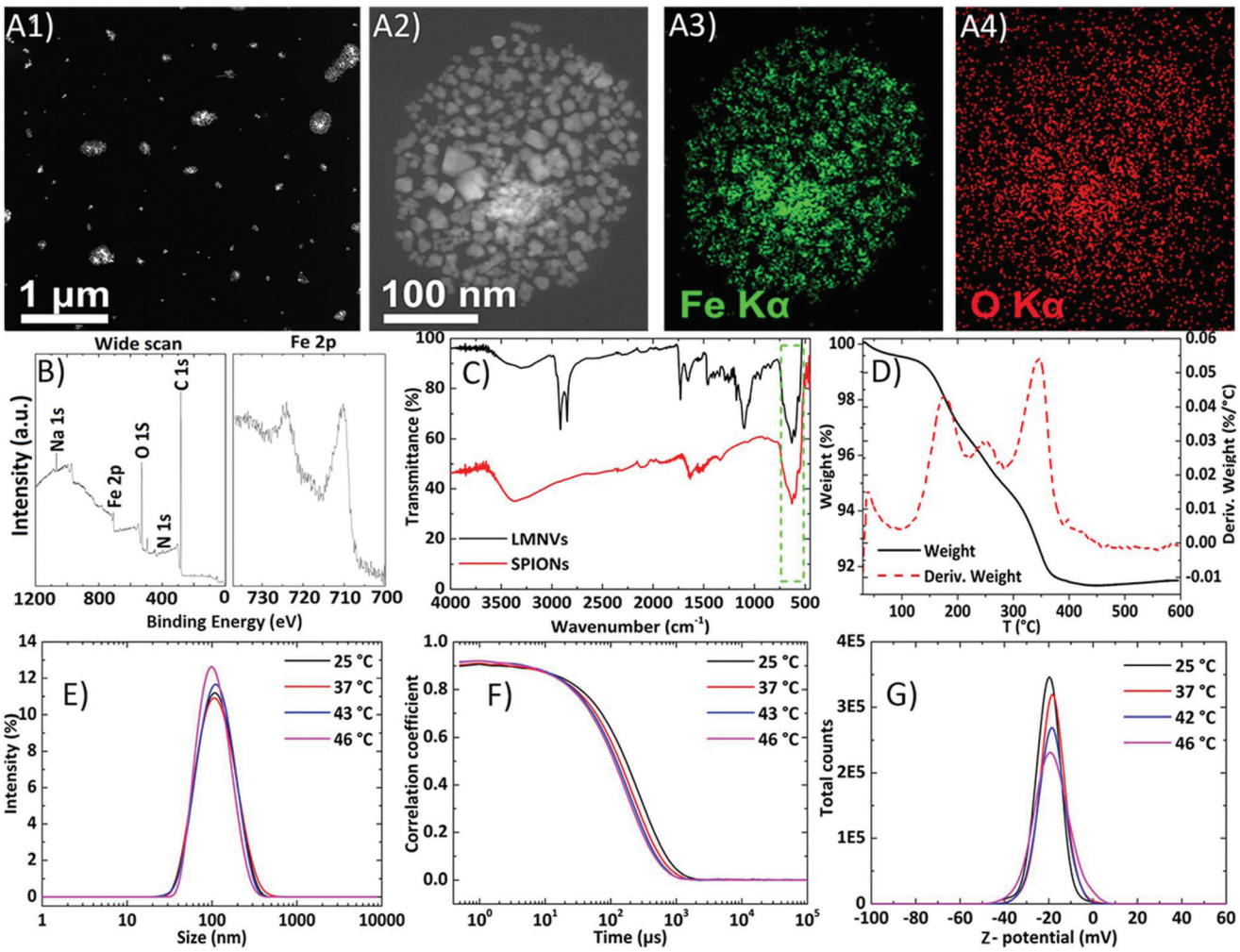

Fig. 1 Morphological and physicochemical characterization of LMNVs: (A1) high-angle annular dark field-scanning transmission electron microscopy (HAADF-STEM) image of LMNVs, (A2) magnified HAADF-STEM image of one unstained LMNV where the distribution of the encapsulated SPIONs is presented, (A3) and (A4) EDS maps of Fe and O over single LMNV, respectively; (B) XPS graph demonstrating the elements present on the surface of the LMNVs; (C) FT-IR spectra of plain SPIONs (bottom) and LMNVs (top) showing peaks attributed to the SPIONs (Fe–O), depicted inside the green rectangular area, and to the lipid components; (D) TGA/DTA graph presenting the weight reduction of the LMNVs during the melting of the lipids and of the polymeric components of the LMNVs (black curve). The red dashed line represents the derivative weight in which each peak represents transition temperatures (melting points) attributed to both the lipid matrix and the incorporated PEG; (E) Gaussian distributions of the hydrodynamic diameter (100 nm) of the LMNVs at various temperatures; (F) correlograms of the LMNVs at various temperatures demonstrating the stability of the LMNVs; (G) surface charge (about –19 mV) of the fabricated LMNVs at various temperatures.

EDS analysis (Fig. S2†) and we calculated the percentage per weight of each element. The results demonstrate the presence of C (24.6%), O (35.13%), and Fe (40.14%), proving the existence of a lipid as well as of an iron-based component.

The surface of LMNVs was characterized using X-ray photoelectron spectroscopy (XPS) (Fig. 1B) from which it was found that the percentage of Fe on their surface comprises 0.8% of the surface elements (C: 81.6%, O: 15%, N: 0.6%, Na: 1.0, Cl: 0.2%, Si: 0.7%). Analysis of the binding energy region between 700 eV and 740 eV, typical of Fe 2p peaks, revealed the presence of Fe $2p_{3/2}$ and Fe $2p_{1/2}$ peaks at approximatively 710.4 eV and 724.1 eV, respectively; importantly, the collected data do not show the presence of any well-defined satellite peak in the region between the two XPS peaks. The observed positions, together with the absence of the satellite peak, are in good agreement with results reported in a previous study[21] on Fe_3O_4.

Infra-red spectroscopy was also used as a complementary technique to verify the presence of SPIONs inside the LMNVs. The spectra of the SPIONs as well as of the LMNVs are presented in Fig. 1C. The peaks in the range of 550–600 cm^{-1} that are visible both in the spectra of SPIONs (bottom) and of LMNVs (top) can be attributed to the vibrations between Fe and O of the encapsulated SPIONs. The peaks at 1100 cm^{-1} and at 1730 cm^{-1} that can be seen only in the LMNV spectrum (Fig. 1C – top) are attributed, respectively, to the C–O and C═O stretching vibrations of the aliphatic chain of the lipids. The peaks at 2841 cm^{-1} and 2914 cm^{-1} in the LMNVs spectrum belong to the C–H stretching vibrations of the aliphatic chain, while the broad peaks in the range of 3100–3500 cm^{-1}, which can be seen in both spectra, are attributed to O–H stretching vibrations.

The total percentage of Fe inside the LMNVs as well as the amount of SPIONs inside the LMNVs were calculated using inductively coupled plasma optical emission spectroscopy (ICP-OES) and thermogravimetric analysis (TGA), respectively. The ICP-OES results showed that Fe represents 66.8% of the LMNVs, while thermogravimetric analysis demonstrated that 88% of the LMNVs are composed of SPIONs. Thermogravimetric analysis of the LMNVs was carried out in order to calculate the percentage of encapsulated SPIONs, as well as to evaluate any structural changes related to temperature alterations. Fig. 1D depicts both the weight loss and the differential thermogravimetric curve of the LMNVs. From these curves, the structural deformation as well as the decomposition of the lipid and of the polymeric part of the nanostructure are evident. When the temperature is above 50 °C, a weight loss can be observed, which can be attributed to water molecules trapped on the surface of the LMNVs (50–100 °C), as well as due to the decomposition of the GMS, mPEG-DSPE (methoxy-poly(ethylene glycol)-1,2-distearoyl-*sn*-*glycero*-3-phospho-ethanolamine), and DPPC (1,2-dipalmitoyl-rac-*glycero*-3-phosphocholine). This loss is achieved in multiple steps as can be observed from the differential thermal analysis graph, where three peaks are presented (Fig. 1D). The first peak can be attributed to the degradation of the poly(ethylene glycol) chain derived from mPEG-DSPE, while the second one can be attributed to the release of energy due to the structural deformation resulting from the parallel decomposition of all the lipid components. Finally, the third peak can be attributed to the degradation of GMS. Above 380 °C, it can be observed that there is no further weight loss due to the fact that both the polymeric and the lipid coating have been completely degraded. The remaining weight can be attributed to the encapsulated SPIONs and corresponds approximately to 88% of the initial weight as was mentioned before.

Stability studies

The stability of the LMNVs was studied in media with different conductivities and ionic strengths, and at different temperatures, in order to assess their behavior under conditions that simulate the cancerous environment, as well as conditions that simulate their exposure to hyperthermia treatment (T > 42 °C). In addition, the stability of the LMNVs in relation to protein corona formation was also assessed by studying their behavior in Dulbecco's modified Eagle's medium (DMEM) supplemented with 10% fetal bovine serum (FBS).

The results presented in Fig. 1E demonstrate that the LMNVs are stable as the temperature increases from 25 °C to 46 °C, maintaining an average hydrodynamic diameter (R_d) of 106.2 ± 13.0 nm and a polydispersity index (PDI) of 0.206 ± 0.030. The correlograms presented in Fig. 1F demonstrate a good decay time and a flat line at the end of the curves for all the samples, proving the absence of sedimentation over time and over temperature increment, as well as the absence of aggregation. The average Z-potential value of the LMNVs, at various temperatures (Fig. 1G), was found to be −19.0 ± 1.3 mV. Although this value is higher than −30 mV, which is considered the threshold for the colloidal stability of a system, our fabricated nanovectors demonstrated excellent stability, both in water and in biologically simulated fluids (DMEM + 10%FBS). This behavior can be attributed to the synergic effect of the electrostatic repulsion due to the negative surface charge of the LMNVs, as well as to the steric hindrances due to the incorporated PEG.

The hydrodynamic diameter values in dynamic light scattering (DLS) are higher compared to the diameters presented in TEM, and this difference can be attributed to the PEG segment that creates a layer around the particles, which swells when inside the liquid dispersant, resulting in increased values of the hydrodynamic diameter.

After assessing the stability of the LMNVs at different temperatures, we studied their behavior in different dispersants which more accurately simulate the conditions inside the human body (see ESI, Fig. S3†). Water was used as a control since, in our previous measurements, it was used to prove the temperature-dependent stability of the LMNVs. The other two dispersants that were used were DMEM and DMEM supplemented with 10% FBS (DMEM + 10%FBS). The hydrodynamic diameter graphs (see ESI, Fig. S3† – top) and the correlograms (see ESI, Fig. S3† – bottom) show that the LMNVs

are stable in water after 1, 6 and 24 h at 37 °C, further proving their stability for a longer period than 6 h. In these graphs it can also be observed a significant difference between LMNVs in DMEM and LMNVs in DMEM + 10%FBS, a difference that can be attributed to the protein corona formation around the LMNVs, mostly due to the albumin inside the serum. The protein corona is evident at all the time points, since the size distribution of the nanovectors in the DMEM + 10%FBS (blue curves) is always shifted on the right (higher hydrodynamic diameters) compared to the LMNVs dispersed in ultrapure water (black curves). This difference between DMEM + 10%FBS and water is not evident from the corresponding correlograms, but the difference between these dispersants and the plain DMEM is pretty clear. Plain DMEM graphs present always higher values of hydrodynamic diameter, and this is because the high ionic strength of the media results in aggregates as it can be seen from the graphs in ESI, Fig. S3,† where the curves belonging to the LMNVs dispersed in DMEM (red curves) are shifted to higher hydrodynamic values and present higher intensity. This higher intensity can also be observed in the curves belonging to the LMNVs dispersed in water after 6 and 24 h, suggesting that an aggregation may occur.

In order to further assess the stability of the nanovectors and to assess the probable creation of aggregates in water as well as in DMEM and DMEM + 10%FBS, we performed nanoparticle tracking analysis (NTA) in all of the dispersants after 24 h. Using this method we were able to assess the behavior of the nanovectors in a liquid under flow, observing each particle separately, since NTA has the ability to record the movement of each dispersed particle passing through a high resolution camera with a specific speed. The results that are presented in ESI, Fig. S4 and Table S1† demonstrate that there is an aggregation of the LMNVs in water after 24 h (see ESI, Fig. S4† – black curve, and Table S1† – D50 and D90 values) which cannot be seen in the DLS graphs due to the limitations of the equipment. From Fig. S4 and Table S1† it can also be seen that the LMNVs in DMEM and DMEM + 10%FBS have lower hydrodynamic diameters compared to water, suggesting firstly that DMEM is not significantly affecting the hydrodynamic values as noticed by the DLS analysis, probably due to the fact that the measurement takes place under flow, and secondly that the LMNVs in DMEM + 10%FBS demonstrate good hydrodynamic values that can be attributed probably to the stability that the protein corona offers to the nanovectors. From these studies it can be concluded that the LMNVs present a higher stability in high ionic strength media when these media are supplemented with proteins like those present in the FBS. Although the high ionic strength destroys the Stern layer of the nanovectors in the medium, these nanovectors remain stable probably due to the electrostatic and/or steric interactions between the protein layers.[22–24]

Magnetic characterization

The magnetic properties of the 3 nm SPIONs before and after their encapsulation in the lipid matrix were studied using a superconducting quantum interference device (SQUID). Considering the hysteresis loops measured at room temperature (Fig. 2A), it has been found that the specific magnetization of the free SPIONs (62 emu g^{-1}) is almost two times higher than that of the LMNVs (32 emu g^{-1}), and this difference can be attributed to the additional mass of the lipid matrix. However, the analysis of the hysteresis at low fields (Fig. 2B) shows that the SPIONs are "magnetically" different with respect to the LMNVs. Free SPIONs have a coercive field of around 10 Oe, while the LMNVs do not present any coercivity (within the limits of precision of the instrument). The absence of coercivity at room temperature is an indication that all the particles inside the lipid matrix are superparamagnetic. However, the presence of a weak coercivity in the SPIONs indicates the presence of a population of blocked particles. In fact the zero-field cooled and field cooled (ZFC–FC) curves of the SPIONs that are presented in Fig. 2C not only exhibit a peak at 200 K that could be correlated with the blocking temperature of the main population of superparamagnetic particles, but they are also separated at room temperature, supporting the presence of a population of blocked particles. In the first instance, the blocking temperature is correlated with the particle size of the SPIONs,[25,26] here 3 nm. This size is too small to explain the blocking temperature of 200 K and even less the presence of blocked nanoparticles at room temperature. In fact, it is more reasonable to consider that the blocking process is correlated to the inter-particle coupling present in the observed aggregates of SPIONs in the pure sample.[25,27,28] In the LMNVs these aggregates of particles were not observed, thus explaining the full superparamagnetic behavior of the particles at room temperature.

In order to assess the ability of the LMNVs to be used in hyperthermia therapy, we studied the increase of temperature in response to an external AMF at various frequencies. The results presented in Fig. 2D demonstrate that 5.4 mg ml^{-1} (66.8% of Fe according to ICP results and 4.8 mg ml^{-1} of Fe_3O_4 according to TGA) of LMNVs can increase the temperature of the dispersant from 27.5 °C to 46.0 °C in 30 min, while the increase from 37.0 °C (human body temperature) to 43.0 °C (mild hyperthermia temperature) can be achieved in a period of approximately 10 min, demonstrating their potential for *in vitro* and *in vivo* use. Data for stimulation using 2.4 mg ml^{-1} of LMNVs are, moreover, provided in the ESI (Fig. S5†).

The effectiveness for the radiofrequency magnetic hyperthermia is quantified by measuring the specific absorption rate (SAR) and the intrinsic loss power (ILP). In both cases the nanoparticles dispersed in the solvent media are exposed to magnetic fields of different intensities as well as of different frequencies. The increase in the first moments of the irradiation allows the determination of the SAR and ILP, while the highest temperature is given at least after 30 min when an equilibrium is reached. The values presented in Table S2 in the ESI† demonstrate that the used LMNVs are superior to their corresponding controls, which are the plain SPIONs (SAR_{LMNVs} = 1345 W g^{-1} *vs.* SAR_{SPIONs} = 678 W g^{-1} at 525 kHz and 20 mT, and SAR_{LMNVs} = 1282 W g^{-1} *vs.* SAR_{SPIONs} = 611 W g^{-1} at 750 kHz and 20 mT). The relationship between

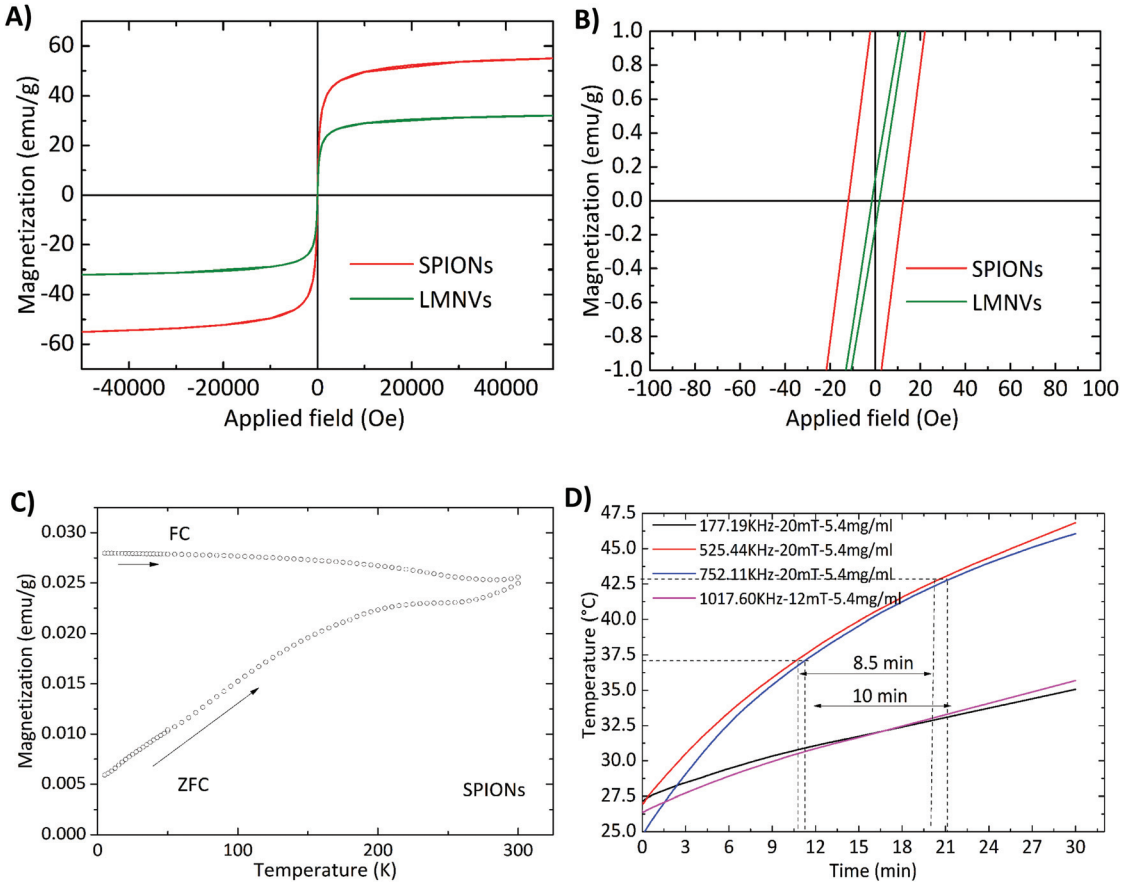

Fig. 2 Magnetic characterization: (A) magnetization curves of plain SPIONs (red curve) and of LMNVs (green curve) where the saturation magnetization can be seen. These curves indicate the superparamagnetic behavior of the LMNVs; (B) magnified images of the hysteresis loops at low magnetic fields where the coercive field is evident and which proves a better superparamagnetic behavior of the LMNVs, since the coercive field of LMNVs is lower than that of the 3 nm SPIONs; (C) ZFC–FC curves of the plain SPIONs, where it is evident that the plain SPIONs do not fully express their superparamagnetic behavior at room temperature, since the two curves are separated at 300 K; (D) response of the LMNVs to an external AMF using various frequencies and magnetic fields for a concentration of 5.4 mg ml^{-1}. From this graph it is evident that at frequencies between 525 and 752 kHz it is possible to reach the temperature of 43 °C, and that this temperature can be reached in 8.5 min when specific frequencies are used.

magnetic hyperthermia and inter-particle interactions/particle aggregation is a subject of debate, given the contrasting results found in the literature.[29–32] The samples here investigated are composed of very small magnetic nanoparticles, 3 nm, and the increased SAR values that the LMNVs present can be attributed to the fact that these nanoparticles are more stable (as was demonstrated by the dynamic light scattering studies) and do not aggregate, as well as to the fact that probably the SPIONs inside the lipid-based matrix act as a single structure, resulting into a synergic effect that enhances SAR. It has to be noted that the SAR values presented in this paper are higher than those of other studies presented in the literature,[33,34] taking into consideration the experimental conditions. In addition, it should be emphasized that the fabricated LMNVs have the ability to increase apoptosis by 50% under a specific treatment, as shown later, and this can be possibly attributed to the fact that the LMNVs generate a localized intracellular hyperthermia that results in cell death through apoptotic mechanisms, as also reported by other groups.[35–38] The ILP values were calculated and reported in Table S2† in order to make easier the comparison of our system with other systems in the literature that use different equipment and measures of the effectiveness of their magnetic-based structures.

Loading and release studies

The percentage of the loaded TMZ (%DL) was found to be 4.1 ± 0.5% (w/w), and was calculated after the extraction of the drug from the nanovectors using the procedure described in the 'Materials and methods'. After calculating the dynamic loading, we calculated the encapsulation efficiency, %EE = (weight of the encapsulated TMZ/total weight of TMZ added) × 100, as well as the yield, %Y = total weight of LMNVs/(total weight of lipids + Fe_3O_4 nanoparticles + TMZ), of the loaded nanovectors, and these percentages were respectively 9.9 ± 2.4% and 17.5 ± 1.0%, percentages which are relatively high compared to similar nanoparticles in the literature.[39,40]

Moreover, it should be noted that the LMNVs presented a pH and an H_2O_2-dependent release, as well as an enhanced

sensitivity to temperature after their exposure to the AMF. The tested pH, 7.4 and 4.5, were used to simulate normal conditions inside the human body as well as the low pH inside the lysosomes. With the same rationale, 50 μM of H_2O_2 was used in order to simulate the overexpressed amount of reactive oxygen species (ROS) in the cancerous cells. The data presented in Fig. 3A and B demonstrate that the LMNVs present a slow and sustained release of TMZ under physiological conditions (3.3% after 7 days at pH 7.4, black square in Fig. 3A), and a slight increase in the release when the pH reduces to 4.5 (8.2% after 7 days, black square in Fig. 3B). When H_2O_2 is added to the system the release of TMZ does not significantly change with respect to the samples that were not treated with H_2O_2, resulting after 7 days in a release of 1.8% at pH 7.4 and of 5.0% at pH 4.5, respectively (red circles). These release percentages are lower with respect to the corresponding samples at pH 7.4 (3.3%, black square in Fig. 3A) and 4.5 (8.2%, black square in Fig. 3B) after 7 days, but this decrement cannot be considered significant, since only a difference of 2.8% after 7 days is observed between the samples treated at pH 4.5 (8.2%) and at pH 4.5 + H_2O_2 50 μM (5.4%), while a difference of 1.9% was found between the samples at pH 7.4 (3.3%) and at pH 7.4 + H_2O_2 50 μM (1.4%). On the other hand, when the samples are exposed to magnetic hyperthermia an increased release that reaches 65.8% at pH 7.4 and 63.3% at pH 4.5 can be observed after 7 days. Even after 4 h, the samples that were exposed to hyperthermia released the majority of their cargo (61.0% for pH 7.4 and 57.6% for pH 4.5), demonstrating the immediate effect of the hyperthermia treatment. It seems that the increase in temperature affects the release of TMZ, and this can be attributed to a possible structural deformation of the lipid matrix when the samples are exposed more than one time to the AMF. This structural deformation can also be affected by the pH as well as by the H_2O_2 that can lead to lipid peroxidation and degradation of the nanovector. Altogether, it should be noted that when these three factors (temperature, pH and H_2O_2) concur, a synergic effect that results in the complete release of TMZ (100%) after 7 days (Fig. 3B), probably due to the complete degradation of the LMNVs, can be observed. On the other hand, when H_2O_2 and hyperthermia are applied at pH 7.4 (Fig. 3A), the release (61.3%) after 7 days is not complete. These results suggest that the fabricated LMNVs are excellent delivery vehicles that will allow the release of the encapsulated therapeutics only when a combination of conditions that can be found only in cancerous environments will be applied.

Internalization studies

The amount of superparamagnetic nanoparticles associated with the cells and their specific localization at subcellular level (internalized into different cell organelles or interfaced to plasma membrane) affect the efficiency and the apoptotic/necrotic pathways related to the magnetothermal stimulation. As an example, magnetothermal heating of lysosomes induces an increase of the lysosomal ROS and causes caspase-1 dependent cell death.[35] The nanoparticle-mediated heating of the plasma membrane is also able to induce apoptosis by acting at membrane rafts, activating the damage-associated molecular pattern (DAMP) and subsequently inducing immunogenic cell death (ICD).[41]

For this reason, before performing magnetothermal stimulation, a detailed investigation on the progressive cell uptake of LMNVs, their association with plasma membranes, and their internalization in acidic organelles was carried out (Fig. 4). Fig. 4A shows confocal laser scanning microscopy (CLSM) imaging of LMNVs (in red), U-87 MG cell membranes (in green), and nuclei (in blue). Qualitatively, an increase of LMNV signal was detected at 72 h of nanoparticle incubation with respect to the 4 h and 24 h time points. Interestingly, the subcellular localization of LMNVs internalized in cells was mostly observed in the cortical region of the cells in proximity of the intracellular side of the plasma membrane, while only a

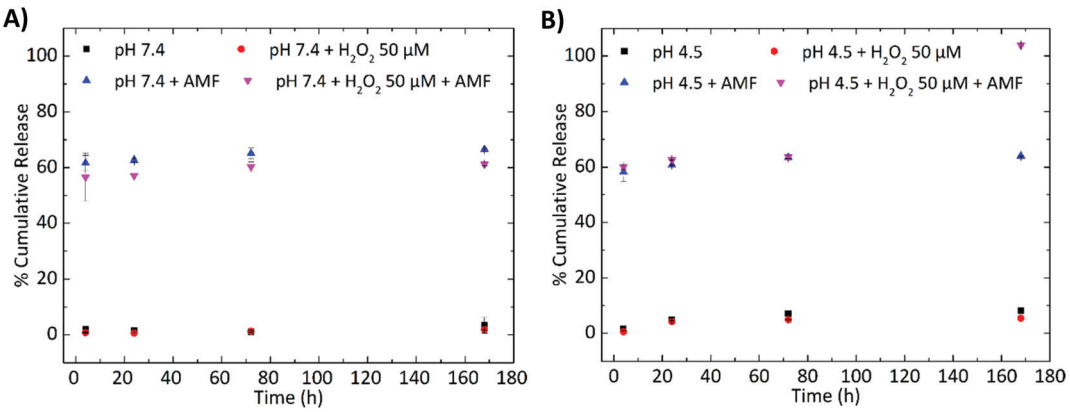

Fig. 3 Release profile of TMZ at various time points (4, 24, 72, and 168 h) and under various treatments at (A) pH 7.4 and (B) pH 4.5. The presented values are given as the mean ± standard error of 3 different measurements. LMNVs present a controlled and sustained release profile when pH is 7.4 and 4.5, while their release profile changes when hyperthermia is applied. The combination of pH and H_2O_2, which is used to simulate the conditions of ROS excess in cancer cells, does not significantly affect the release of TMZ, but the combination of a low pH, which can be found in lysosomes (4.5), an increased H_2O_2 concentration, and hyperthermia leads to 100% release, demonstrating the stimuli-responsive nature of the LMNVs.

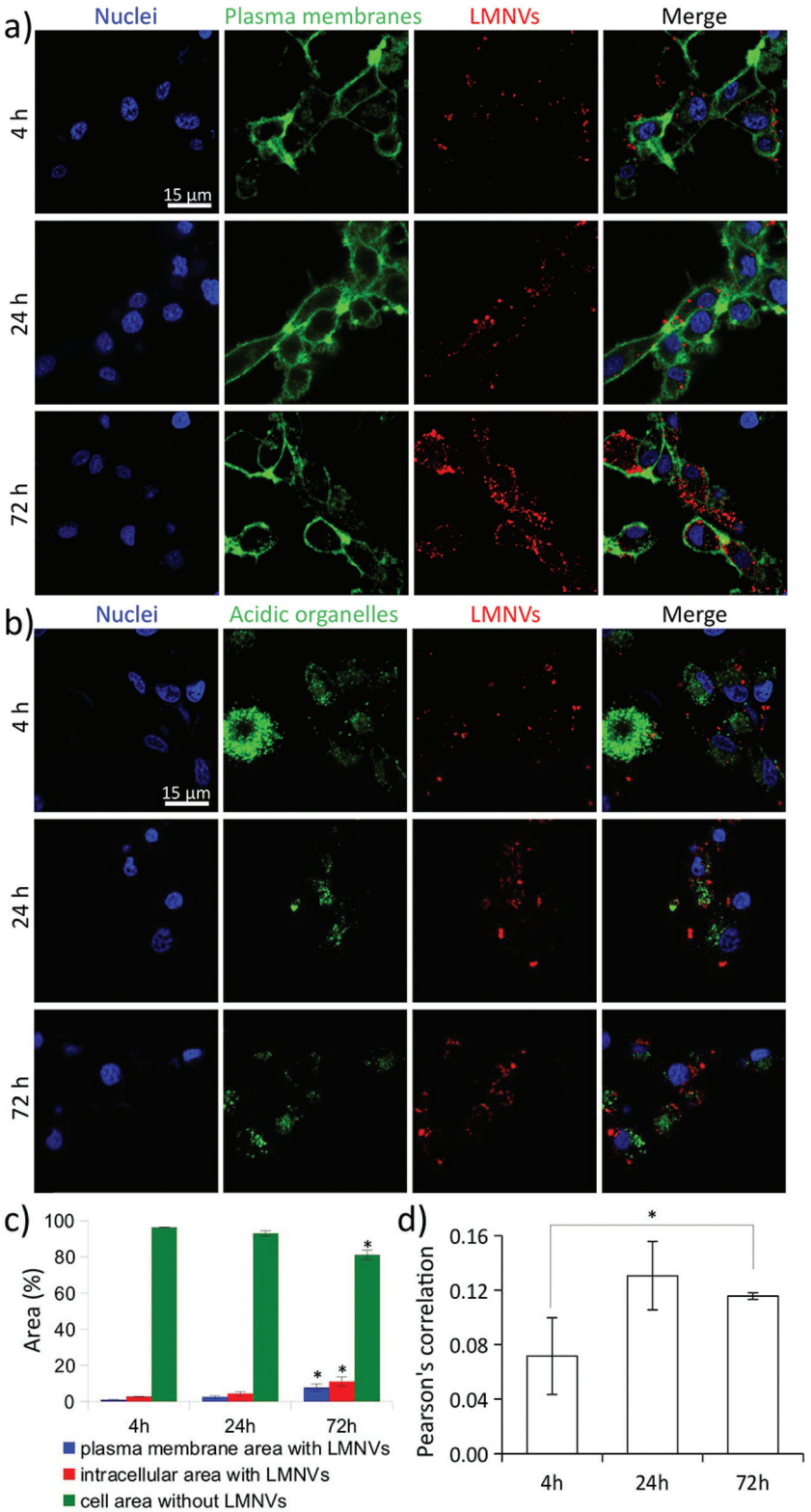

Fig. 4 Investigation of the progressive LMNV uptake by U-87 MG cells: nanovector association with plasma membranes and internalization in acidic organelles at 4, 24 and 72 h of treatment. (A) Confocal laser scanning microscopy (CLSM) imaging of LMNVs (in red), U-87 MG cell membranes (in green), and nuclei (in blue); (B) CLSM imaging of LMNVs (in red), acidic organelles (in green), and nuclei (in blue); (C) histograms presenting the area (%) of plasma membrane signal co-localizing with LMNVs (in blue), of the intracellular region with LMNVs (in red), and of the whole cell (plasma membrane + intracellular region) without LMNVs (in green); (D) histogram presenting Pearson's correlation analysis among the signals of LMNVs and of the acidic organelles. *$p < 0.05$.

small amount was found in the perinuclear region, most probably because of their lipophilic nature.[42] The CLSM imaging of LMNVs that is presented in Fig. 4B (LMNVs in red, acidic organelles in green, and nuclei in blue) shows a scarce level of nanomaterial internalization in the acidic compartments at all the different time points (4, 24, and 72 h). However, an increased signal co-localization between LMNVs and acidic organelles was found at 24 h and 72 h of incubation. The increased LMNV internalization during nanoparticle incubation was also confirmed by flow cytometry (Fig. S6†). Indeed, a progressively enhanced fluorescence emission of cells incubated for 0 h ($2.1 \times 10^4 \pm 0.2 \times 10^3$ a.u.), 4 h ($16.9 \times 10^4 \pm 2.9 \times 10^3$ a.u.), 24 h ($60.8 \times 10^4 \pm 10.3 \times 10^3$ a.u.), and 72 h ($77.6 \times 10^4 \pm 9.8 \times 10^3$ a.u.) with DiO-stained LMNVs was observed.

The quantitative analyses of LMNV internalization as well as of their co-localization with the cell membrane and acidic organelle signals are shown in Fig. 4C and D, respectively. The histogram in Fig. 4C indicates the area (%) of plasma membrane signal co-localizing with the LMNVs (in blue), of the intracellular region with LMNVs (in red), and of the whole cell (plasma membrane + intracellular region) without LMNVs (in green). As expected, at 72 h of incubation, a significant increase of the plasma membrane area (7.8 ± 2.0%) and of the intracellular region (11.2 ± 2.6%) containing LMNVs were measured with respect to both 4 h (area of plasma membrane with LMNVs was 1.0 ± 0.1%; intracellular region with LMNVs was 2.7 ± 0.1%; $p < 0.05$) and 24 h (area of plasma membrane with LMNVs was 2.6 ± 0.6%; intracellular region with LMNVs was 4.4 ± 1.0%; $p < 0.05$) treatments. At the 72 h time point, a relatively large amount of the total cell area (plasma membrane + intracellular region) was occupied by LMNVs (19.0 ± 4.5%), compared to the 4 h (3.7 ± 0.2%) and to the 24 h (7.0 ± 1.5%) time points. The histogram presented in Fig. 4D shows Pearson's correlation analysis among the signals of LMNVs and of the acidic organelles. A significant, yet low, increase of signal co-localization was found just at 72 h (0.116 ± 0.003) compared to 4 h (0.071 ± 0.008; $p < 0.05$), thus indicating a progressive slow internalization of LMNVs in acidic compartments. No significant differences were found at the 24 h intermediate time point (0.130 ± 0.025; $p > 0.05$) with respect to the other time points.

Cytotoxicity studies

In order to assess the cytotoxic effect of the fabricated LMNVs, cell proliferation studies using the WST-1 assay were performed. LMNVs, TMZ-LMNVs and free TMZ that correspond to the amount loaded in the LMNVs were tested at various concentrations (100, 200, 400 and 800 μg ml^{-1} for the nanovectors and 2.2, 4.4, 8.75 and 17.5 μg ml^{-1} for the free TMZ, respectively) and at two time points (24 and 96 h). The results presented in Fig. S7A† demonstrate that for the first 24 h the LMNVs do not induce any toxicity even at concentrations up to 800 μg ml^{-1}, while the TMZ-LMNVs cause a reduction of the metabolic activity, compared to the control, at the highest used concentration (800 μg ml^{-1}), which nevertheless is not statistically significant. It has to be noted that the corresponding amounts of free TMZ at 24 h do not induce a reduction in the metabolic activity of the cells, suggesting that the toxicity highlighted in cells after a 24 h treatment with 800 μg ml^{-1} of TMZ-LMNVs can be attributed to an enhanced TMZ cellular uptake. After 96 h it is evident that the metabolic activity of cells treated with plain LMNVs is increased compared to the controls, proving the non-toxicity of the fabricated nanovectors. On the other hand, a reduced increase in the metabolic activity at 96 h at 400 and 800 μg ml^{-1} is evident for the cells treated with TMZ-LMNVs, and this decrease can be attributed to an enhanced delivery of TMZ inside the cells. A reduced metabolic activity is finally evident in cells treated with free TMZ, proving its anti-proliferative ability, which is enhanced when loaded inside the presented nanovectors as stated above. Cytotoxicity studies were also performed with and without the exposure of free TMZ, LMNVs and TMZ-LMNVs in an alternating magnetic field, and the results are given in the following paragraph.

Chronic AMF stimulation

The effects of drug-loaded LMNV (TMZ-LMNVs)-assisted magnetothermal treatment were investigated on U-87 MG cells after 4 days of AMF treatment (2 h per day) by analyzing the apoptotic levels with flow cytometry analysis following annexin V-FITC/PI staining, the expression of the Ki-67 proliferation nuclear marker and of the p53 tumor suppressor marker (Fig. 5), and the cell culture metabolism through the WST-1 assay (see ESI, Fig. S7B†). Eight different experimental conditions were considered for these experiments: non-treated control cultures exposed or not to AMF (named "Control + AMF" and "Control", respectively), cultures treated with 8.75 μg ml^{-1} TMZ (amount corresponding to 400 μg ml^{-1} of TMZ-LMNVs) and exposed or not to AMF (named "TMZ + AMF" and "TMZ", respectively), LMNV-incubated cultures exposed or not to AMF stimulation (named "LMNVs + AMF" and "LMNVs", respectively), and finally, TMZ-LMNV-treated cultures exposed or not to AMF stimulation (named "TMZ-LMNVs + AMF" and "TMZ-LMNVs", respectively). Fig. 5A shows the flow cytometer scatter plots (PI *vs.* annexin V-FITC) and representative confocal images of the immunostaining of p53 expression (in green), and of Ki-67 expression (in red) for each experimental condition; in all fluorescence images nuclei are counter-stained in blue. We observed that the chronic AMF stimulation was able to affect the viability and the proliferation levels of U-87 MG cells only in the presence of LMNVs or TMZ-LMNVs. Indeed, higher annexin V-FITC fluorescence emissions (apoptotic populations are highlighted in magenta) in concomitance with a higher expression of the p53 tumor suppressor marker and lower levels of the Ki-67 proliferation marker were found in both LMNVs + AMF and TMZ-LMNVs + AMF, with respect to the other experimental groups. A higher nuclear expression of p53 (prevalently cytoplasmatic in control cultures) was detected in both LMNVs + AMF and TMZ-LMNVs + AMF groups compared to the untreated samples, which was followed by a prominent decrease of cell number. No relevant differences were found

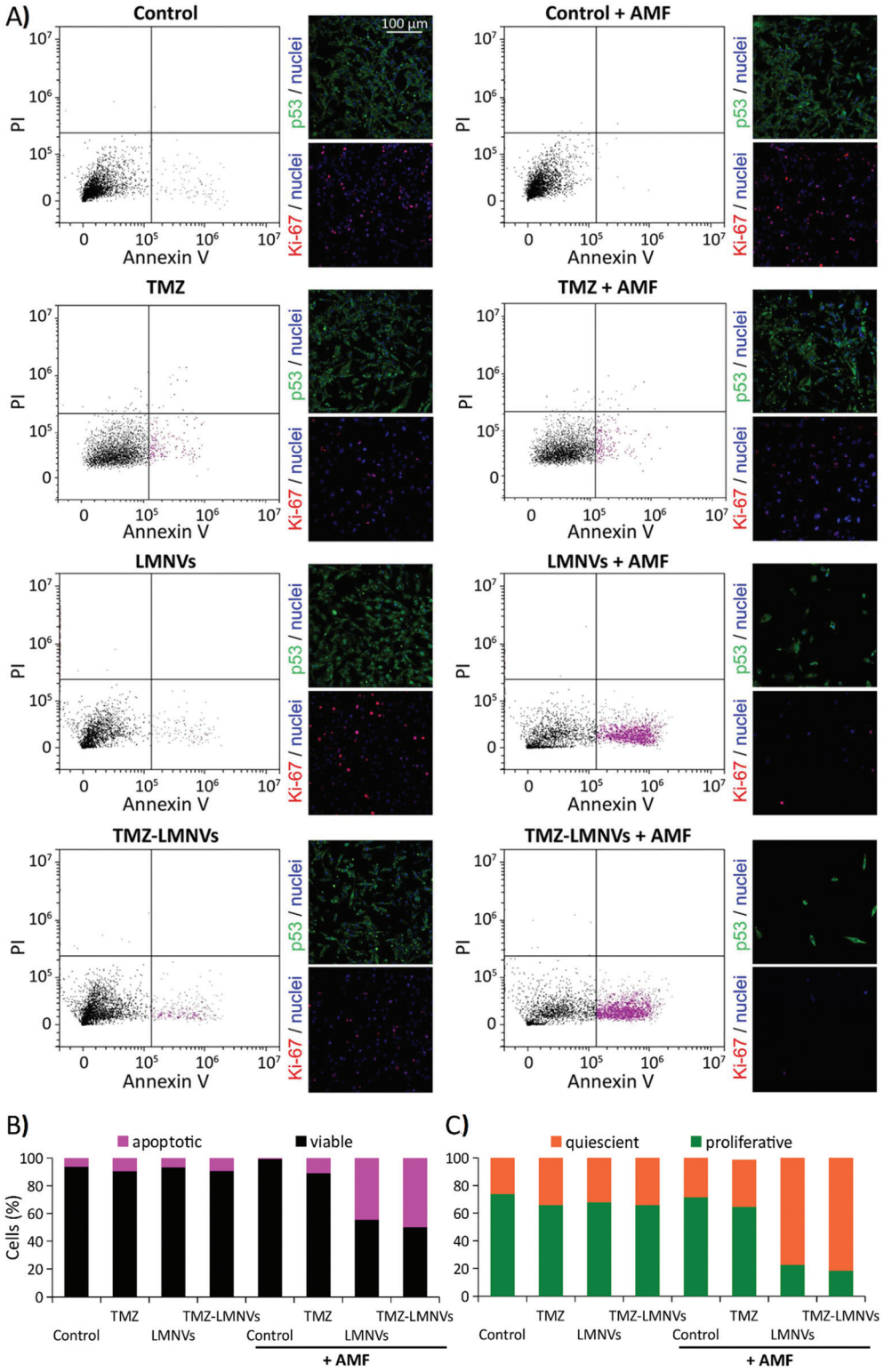

Fig. 5 Chronic magnetothermal treatment induces apoptosis, inhibits proliferation, and drastically reduces the U-87 MG cancer cell number. (A) Flow cytometer scatter plots (propidium iodide *vs.* annexin V-FITC) and confocal images of p53 expression (in green), Ki-67 expression (in red) and nuclei (in blue) for untreated cells (CTRL), for cells treated with free TMZ, cells treated with plain LMNVs, and cells treated with TMZ loaded LMNVs (TMZ-LMNVs), with (+AMF) and without (–AMF) exposure to an alternating magnetic field. Apoptotic populations in the scatter plots are highlighted in magenta. (B) Histograms reporting the percentage of viable (in black) and annexin V^+ apoptotic (in magenta) cells for each experimental condition. (C) Histogram presenting the percentage of proliferating cells (in green) and of quiescent cells (in orange) following Ki-67 expression evaluation.

among the Control + AMF and Control groups. This result reveals the safety of the AMF approach contemplated for the local stimulation of LMNV-treated cancer cells. Qualitatively, a small increase of the annexin V^+ cells and of $p53^+$ nuclei was detected in TMZ-LMNVs compared to the control and to the LMNV experimental groups, probably due to the non-specific release of TMZ from the drug-loaded vectors. Moreover, a small increase of annexin V^+ cells and of $p53^+$ nuclei was detected in TMZ-LMNVs, TMZ and TMZ + AMF groups compared to the Control and to the LMNV experimental groups, thus confirming the pro-apoptotic effects of the drug.

Quantitative analyses are provided in Fig. 5B and C. In Fig. 5B the histogram related to the percentage of viable (in black) and annexin V^+ apoptotic (in magenta) cells for each experimental condition is reported. The percentages of apoptotic cells in the entire population that was treated with LMNVs + AMF (44.5%) and with TMZ-LMNVs + AMF (50.0%) were significantly higher with respect to Control (6.4%), Control + AMF (0.6%), TMZ (9.4%), TMZ + AMF (10.8%), LMNVs (6.6%) and TMZ-LMNVs (9.3%) groups ($p < 0.05$). Single distributions are reported in ESI, Fig. S8.†

The histogram of Fig. 5C reports the percentage of proliferative cells (in green) and of quiescent cells (in orange) for each of the eight experimental groups, evaluated after Ki-67 staining. The percentage of proliferative cells in LMNVs + AMF (22.6 ± 1.0%) and in TMZ-LMNVs + AMF (18.2 ± 2.4%) groups are significantly lower with respect to Control (73.8 ± 1.1%), Control + AMF (71.3 ± 2.2%), TMZ (64.6 ± 1.9%), TMZ + AMF (65.9 ± 0.9%), LMNVs (67.9 ± 5.0%) and TMZ-LMNVs (65.75 ± 1.18%) groups ($p < 0.05$). The best results in terms of apoptotic and anti-proliferative effects were observed in the TMZ-LMNVs + AMF group, thus highlighting the effectiveness of the synergic treatment using magnetothermal stimulation and chemotherapy.[34]

Coherently with the smaller number of cells revealed in TMZ-LMNVs + AMF and LMNVs + AMF treated cultures, analysis of WST-1 absorbance showed a remarkable ($p < 0.005$) decrease of cell metabolism under these two experimental conditions (11.4 ± 0.2% for TMZ-LMNVs + AMF; 15.4 ± 0.3% for LMNVs + AMF) compared to all the other experimental groups: Control (100.0 ± 1.9%), Control + AMF (106.1 ± 0.7%), LMNVs (104.7 ± 1.8%), and TMZ-LMNVs (62.7 ± 3.1%). A small, yet significant ($p < 0.05$), decrease could also be observed after 96 h between the untreated samples (Control and the Control + AMF) and samples treated with temozolomide (TMZ, 82.4 ± 3.4%, and TMZ + AMF, 78.8 ± 7.9%); however these values are still significantly higher with respect to those found for the LMNVs + AMF and TMZ-LMNVs + AMF groups, as reported above.

It is important to highlight that the results acquired from cell metabolism tests are in agreement with the apoptotic evaluation, showing better anticancer performances after the TMZ-LMNVs + AMF combined treatment. Furthermore, cell metabolism analysis in TMZ-LMNVs samples highlighted a lower metabolic activity compared to Control, Control + AMF, and LMNV experimental classes, confirming thus the anticancer effect of TMZ in U-87 MG cells.[43]

Preliminary analysis of LMNV crossing an *in vitro* BBB model

The ability of LMNVs to cross an *in vitro* BBB model was preliminarily investigated (Fig. 6), as previously reported in the literature.[44] Briefly, two-compartment BBB models consisting of porous scaffolds (with pores of 3 μm diameter) were used to culture brain endothelial cells (BEC) at high confluence. The developed endothelial layer completely covered the porous scaffold, separating the luminal chamber (on the top) by the abluminal compartment (on the bottom), and was characterized by a sustained expression of the tight junction marker *zonula occludens-1* (ZO-1; Fig. 6A). The BBB model showed a transendothelial electrical resistance (TEER) of 42 Ω cm^2 and its permeability to 50 μg ml^{-1} of FITC-dextran (4 kDa) was significantly lower with respect to the plain porous scaffold (without cells; Fig. 6B; $p < 0.05$).

A progressive crossing of DiO-stained LMNVs through the BBB was detected when treating the luminal compartment of the BBB model with 1.3 mg ml^{-1} of DiO-stained LMNVs (Fig. 6C), with 7.00 ± 1.82 μg, 22.00 ± 1.40 μg and 52.00 ± 8.96 μg crossing the abluminal compartment at, respectively, 4, 24 and 48 h of incubation. Fig. 6D shows the fluorescence emission distributions derived from flow cytometry analysis of U-87 MG cells seeded in the abluminal compartment at 4, 24, and 48 h of incubation with DiO-stained LMNVs in the luminal chamber. It is possible to appreciate a progressive shift of the distributions to higher values of fluorescence emission by increasing the incubation time: the percentage of $LMNV^+$ cells was 0.5%, 3.3% and 16.5% at, respectively, 4, 24 and 48 h of incubation. Fig. 6E shows representative CLSM imaging of U-87 MG cells (f-actin in red, nuclei in blue) in the abluminal compartment after 48 h of incubation with DiO-stained LMNV in the luminal chamber.

These preliminary results concerning the ability of LMNVs to cross the BBB are certainly promising, and pave the way to testing the efficiency of the presented nanovectors on more relevant *in vivo* GBM models for preclinical evaluations.

Materials and methods

Preparation of lipid-based magnetic nanovectors

25 mg of 1-stearoyl-rac-glycerol (Sigma-Aldrich), 2.5 mg of oleic acid (Sigma-Aldrich), 2.5 mg of 1,2-dipalmitoyl-rac-*glycero*-3-phosphocholine (Sigma-Aldrich), 4 mg of mPEG-$DSPE_{5k}$ (Sigma-Aldrich), and 2.5 mg of temozolomide (Sigma-Aldrich) (when TMZ-LMNVs are fabricated), are mixed with 84.5 μl of an ethanol solution of superparamagnetic iron oxide nanoparticles (15 wt%; US Research Nanomaterials Inc.), inside a 6 ml glass vial. Subsequently, the vial is placed inside an ultrasonic bath (Elmasonic S 35w) set at 70 °C in order to melt the lipids and to allow ethanol to evaporate. After ethanol evaporates, 3 ml of a pre-warmed (70 °C) Tween® 80 (Sigma-Aldrich) solution (1.0 wt%) were added to the lipid mixture and immediately sonicated using an ultrasonic homogenizer (Fisherbrand™ Q125 Sonicator) for 15 min (amplitude 30%, 120 W). After the ultrasonic homogenization, the hot mixture is transferred to a high pressure homogenizer (HPH, EmulsiFlex-B15 from Avestin), where the sample is further homogenized by

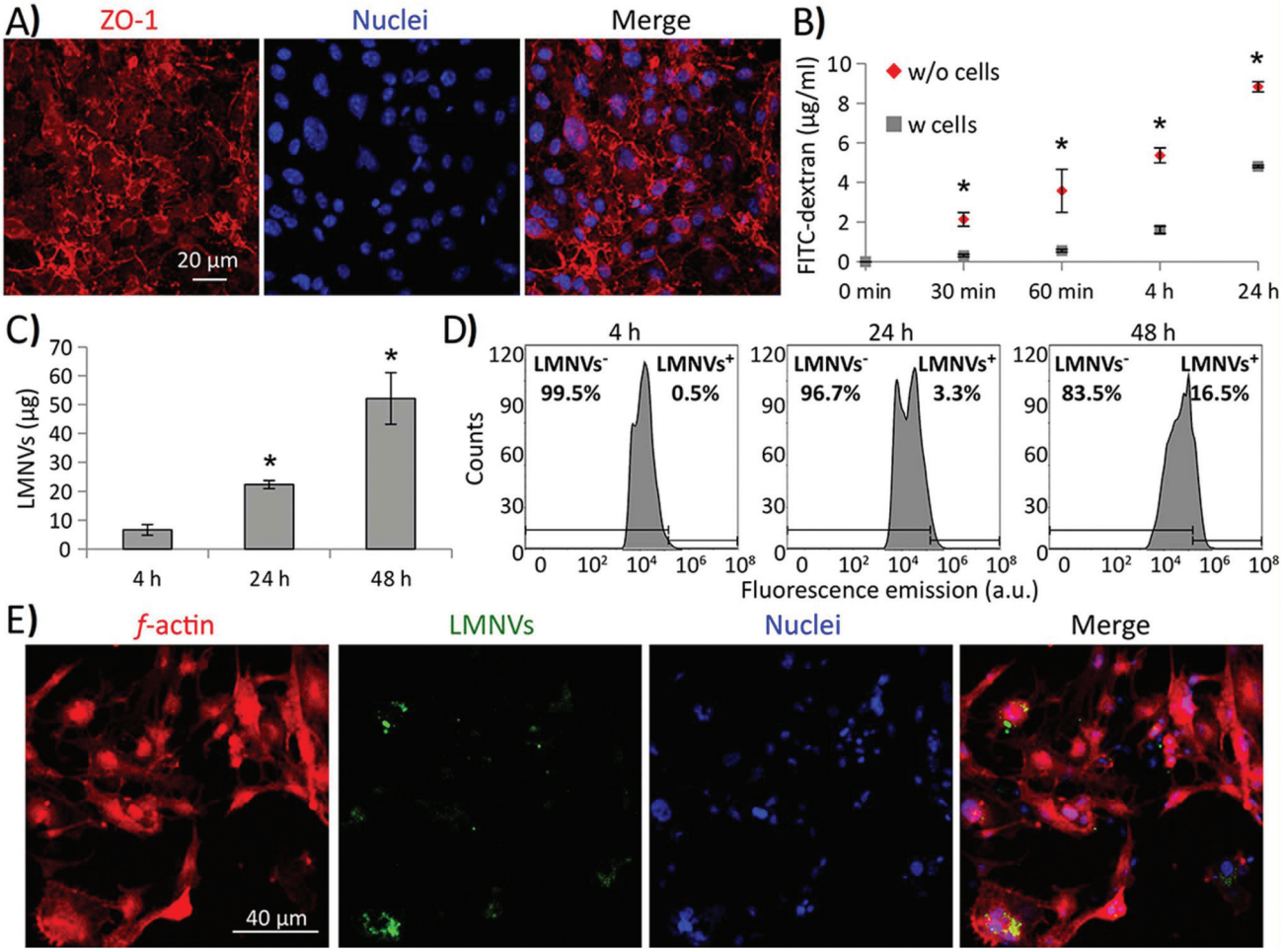

Fig. 6 Ability of LMNVs to cross an *in vitro* BBB model. (A) Expression of the tight junction marker *zonula occludens-1* (ZO-1 in red, nuclei in blue); (B) crossing of the BBB (with cells; in gray) and of the plain porous scaffold (without cells; in red) of 4 kDa FITC-dextran used as a model substance; (C) progressive crossing of DiO-stained LMNVs through the BBB model after treating the luminal compartment with 1.3 mg ml^{-1} of DiO-LMNVs; (D) fluorescence emission distributions of U-87 MG cells seeded in the abluminal compartment at 4 h, 24 h, and 48 h of incubation with DiO-stained LMNVs in the luminal chamber, showing the progressive uptake of the DiO LMNVs by the U-87 MG cells; (E) representative CLSM images of U-87 MG cells (f-actin in red, nuclei in blue) in the abluminal compartment after 48 h of incubation with DiO-stained LMNV incubation in the luminal chamber. *$p < 0.05$.

passing it 5 times through the homogenizer at a pressure of 100 000 psi. After the homogenization, the LMNVs are placed for 30 min at 4 °C to allow the lipid-based structures to stabilize. The LMNVs are purified by centrifugation and washing with ultrapure (Mili-Q) water (3 times for 30 min at 4 °C).

Morphological and physicochemical characterization

Electron microscopy and elemental analysis. The morphological characterization of the nanovectors was performed in the high-angle annular dark field-scanning transmission electron microscopy (HAADF-STEM) imaging mode using an image-aberration-corrected TEM JEOL JEM-2200FS instrument, operated at 200 kV. EDS mapping was carried out using a Bruker XFlash 5060 silicon-drift detector (SDD) with 60 mm^2 effective area. For the quantification of the elements, the analysis was performed using an SEM FEI 200 equipped with a Bruker Nano XFlash 5010 detector. Sample preparation was performed by casting 20 µl of a concentrated sample on a silicon substrate and dried on air. Afterwards, the dried sample was coated with gold and placed under examination, using a voltage of 20 keV and a current of 83 pA. The quantification of the elements was performed using Esprit 1.9 software after excluding the peaks attributed to silicon (Si) and gold (Au).

X-Ray photoelectron spectroscopic analysis. XPS measurements were performed using a Kratos Axis Ultra DLD spectrometer using a monochromatized Al Kα source operating at 15 kV and 20 mA. Wide scans were performed at an analyzer pass energy of 160 eV, while high-resolution narrow scans were performed at a constant pass energy of 10 eV and steps of 0.1 eV. The photoelectrons were detected at a take-off angle of $\phi = 0°$ with respect to the surface normal. The pressure in the analysis chamber was maintained below 7×10^{-9} Torr for data acquisition. The data were converted to VAMAS format and processed using the CasaXPS software, version 2.3.17.

Fourier-transformed infra-red spectroscopy. Attenuated total reflection Fourier-transformed infra-red spectroscopy (ATR-FTIR) was performed using a Shimadzu Miracle 10. Before the measurements, all the samples were freeze-dried and a small amount of each dried sample was placed on the diamond surface of the IR cell. The number of scans was set at 45, the scanning range was set at 4000 to 400 cm^{-1}, and the resolution step at 4 cm^{-1}. The graphs were plotted using OriginPro software v. 9.1.

Inductively coupled plasma analysis. The ICP elemental analysis was carried out *via* inductively coupled plasma optical emission spectroscopy (ICP-OES) using an iCAP 6300 DUO ICP-OES spectrometer (Thermo Scientific) operating at an RF power of 1150 W, using a flush pump rate of 100 rpm, an auxiliary gas flow rate of 0.5 l min^{-1} and an analysis pump rate of 45 rpm. The samples were dissolved overnight in HCl/HNO_3 at 3 : 1 (v/v) and diluted with Milli-Q before analysis.

Thermogravimetric analysis (TGA). TGA was performed on small samples (5 mg) using a Q500 analyzer from TA Instruments. The scans were performed in the range of 30–600 °C, using a 10 °C min^{-1} heating rate. Cooling was achieved using 50 ml min^{-1} nitrogen flow.

Dynamic light scattering. Dynamic light scattering measurements were performed using a Zeta-sizer NanoZS90 from Malvern Instruments Ltd. The measurements were carried out at various temperatures (25, 37, 42 and 46 °C) and in media with different pH, and conductivity, and different supplements (H_2O, DMEM (Sigma-Aldrich), and DMEM + 10%FBS). For the hydrodynamic diameter measurements the concentration for all the samples was adjusted to 100 μg ml^{-1}. The Z-potential measurements were carried out in ultrapure water at pH 5.5 and the conductivity was adjusted to the range of 30–100 μS cm^{-1}. The attenuation of the samples during measurements was approximately 9. The surface charge measurements represent the mean ± standard deviation of 3 different measurements with 17 runs for each of them. Before each measurement, the samples were sonicated for ~10 s using a Bandelin ultrasonic probe at 8 W to avoid the presence of aggregates.

Magnetic characterization

The magnetic properties of the plain SPIONs as well as of the LMNVs were measured using a superconducting quantum interference device (SQUID) from Quantum Design. Hysteresis loops were measured from −50 to 50 kOe at 5 K and 300 K upon zero field cooling. The temperature dependence of the magnetization from 5 to 300 K after zero-field cooling (ZFC) and after field cooling (FC) was recorded by applying a probe field of 25 Oe to evaluate the superparamagnetic behavior of the nanoparticles.

Magnetic hyperthermia. Magnetic hyperthermia was performed using a MagneTherm™ equipment from NanoTherics. The applied AMF ranged from 12 mT to 20 mT and the frequencies ranged from 177 kHz to 1017 MHz. The samples were place inside a 2 ml Nalgene tube, which was inserted inside a polystyrene case in order to reduce thermal fluctuations. The polystyrene case with the sample was placed inside a round coil of 9 mm with 44 turns and the hyperthermia measurements lasted from 30 min to 2 h. For the 2 h time point, the sample was exposed 2 times, 1 h each, with 1 min of pause of the AMF between the two exposures.

Evaluation of the specific absorption rate (SAR) and of the intrinsic loss power (ILP). SAR and ILP values were calculated for both plain Fe_3O_4 nanoparticles (3 nm) as well as for the LMNVs according to eqn (1) and (2). The amount of plain Fe_3O_4 nanoparticles that were used was 5.0 mg, while the amount of the used LMNVs was 5.7 mg (which, according to TGA, corresponds to 5.0 mg of Fe_3O_4). Both samples, after sonication for 5 min using an ultrasonic probe (Fisher Scientific, 120 W, 90% amplification), were placed at a final volume of 100 μl inside typical NMR tubes. The tubes were placed exactly in the center of the coil (9 turn, 44 mm), and the temperature was recorded every 1 s using an OSENSA single channel optic fiber. For the calculation of SAR and ILP values the temperature difference that was used was 6 °C and corresponded to the difference between 37 °C and 43 °C. The equations used for the calculation of the above parameters are given below. For further details see ESI, Table S2.†

$$\mathrm{SAR} = C_\mathrm{p} \cdot \frac{D_\mathrm{c}}{C_\mathrm{Fe}} \cdot \frac{\mathrm{d}T}{\mathrm{d}t} \quad (1)$$

$$\mathrm{ILP} = \frac{\mathrm{SAR}}{f \cdot H^2} \quad (2)$$

C_p is the specific heat capacity of the sample, which in our case is 4.18 J g^{-1} K^{-1}; D_c is the density of the colloid at 25 °C, which is 0.997 g ml^{-1}; C_Fe is the concentration of the magnetic moiety in the solvent, dT is the temperature difference (in K) at the specific measurement time (dt); dt represents the first 20 s above 37 °C, where the difference in temperature is measured; f is the frequency of the magnetic field in Hz and H is the intensity of the magnetic field in A m^{-2}.

Loading and release studies

The loading and the release studies were performed using an HPLC Shimadzu LC-20AT similarly to a previously reported study.[45] The chromatographic separation was carried out using a C-18 column (150 mm × 4.6 mm i.d., 5 μm particle size). The mobile phase consisted of methanol (Sigma-Aldrich) and water containing 1% acetic acid of HPLC grade (Sigma-Aldrich) and pumped in isocratic mode (25% MeOH/70% H_2O) with a flow rate of 0.5 ml min^{-1}. The elution of the analyte was monitored at 328 nm. In order to calculate the percentages of the encapsulated TMZ, as well as the percentages of the cumulative release from the LMNVs, a standard curve using various concentrations of TMZ was prepared. The standard curve was prepared by dissolving 1 mg of TMZ in 1 ml volume of the mobile phase and filtered using a 0.2 μm syringe filter. A concentration range of 0.1–100 μg ml^{-1} was prepared upon further serial dilution. To calculate the loading capacity, 0.25 ml of methanol (MeOH) were mixed with 2.4 mg of TMZ-loaded LMNVs and placed under stirring at 70 °C for 3 h. After stir-

ring, 0.75 ml of cold de-ionized water were added to the MeOH dispersion and the samples were centrifuged at 15 000 rpm for 2 h at 4 °C. The supernatant was collected and measured using the conditions described above. For the release studies, at each time point the samples were centrifuged at 15 000 rpm for 1 h at 4 °C and the supernatant of each treatment solution was removed and replaced with a fresh one. 80 μl of each supernatant were injected into the HPLC and analyzed using the parameters described above. Because the release studies were done in phosphate-buffered saline solution, the standard curve of TMZ was also prepared in the same medium. The temozolomide peak was observed at 5.1–5.3 min.

Cell lines

In this study, the glioblastoma multiforme cell line U-87 MG (ATCC® HTB14™) was used. U-87 MG cells were cultured in T75 flasks using high glucose DMEM (Sigma-Aldrich) supplemented with 10% FBS (Gibco), 1% penicillin/streptomycin (Gibco) and 1% L-glutamine (Gibco), under normal culture conditions (37 °C, 5% CO_2, 100% humidity). For all the experiments the used cells were between passage 10 and passage 20. The medium during culture was changed every two days.

Internalization studies

LMNV internalization in living U-87 MG cells was investigated at different time points (4, 24, and 72 h) through confocal laser scanning microscopy (CLSM) imaging (C2s system, Nikon), as previously described,[46] and by flow cytometry using a Beckman Coulter CytoFLEX. Before incubation, LMNVs were stained with the Vybrant DiD (1,1′-dioctadecyl-3,3,3′,3′-tetramethylindodicarbocyanine, 4-chlorobenzene sulfonate salt) (Thermo Fisher) cell-labeling solution for CLSM, and with Vybrant DiO (3-octadecyl-2-[3-(3-octadecyl-2(3*H*)-benzoxazolylidene)-1-propenyl]-, perchlorate) (Thermo Fisher) for flow cytometry experiments. Briefly, 10 mg of LMNVs were incubated with 5 μl of DiD or DiO for 30 min at room temperature. After the incubation the nanovectors were centrifuged at 15 000 rpm for 60 min at 4 °C; the precipitate was collected and re-dispersed in distilled sterile water. The procedure was repeated two times.

Spectral imaging of DiD-stained LMNVs was performed through CLSM (see ESI, Fig. S9†); Fig. S9A† shows CLSM images of a single DiD-stained LMNV at different emission wavelengths and Fig. S9B† reports the corresponding relative emission spectrum of Fig. S9A,† where the characteristic peak ($\lambda \sim 670$ nm) of the Vybrant DiD lipophilic dye is evident.

In order to investigate the cell uptake of LMNVs and their accumulation inside acidic organelles (*i.e.*, lysosomes and late endosomes), fluorescence staining of the plasma membrane (CellMask Green Plasma Membrane Stain, 1 : 1000 dilution, Invitrogen), of the acidic cell compartments (Lysotracker acidotropic probe, 75 nM, Invitrogen), and of the cell nuclei (Hoechst 33342, 1 μg ml^{-1}, Invitrogen) was carried out in serum-free DMEM at 37 °C. Subsequently, the cells were washed twice with phosphate-buffered saline solution (PBS) (Sigma-Aldrich) and then rinsed with a phenol red-free complete medium.

Acquisition parameters of the scan area, laser power and amplification gain were maintained constant for all the different acquisitions. Finally, images were analyzed by using the NIS-Elements software (Nikon) through a semi-automatic approach. Concerning cell uptake, signals of the plasma membranes and of the LMNVs were selected and measured upon intensity thresholding. The intersection between the two signals indicated the area of the LMNVs associated with the plasma membrane. The intracellular area was defined by selecting the regions of the CLSM image that do not co-localize with the plasma membrane signal and that contain nuclei. The intersection between the areas associated with the intracellular region and the LMNVs was then obtained. Co-localization analysis between the acidic organelles and the LMNVs was assessed by investigating Pearson's correlation parameter at the different time points.

Flow cytometry of cells incubated with DiO-stained LMNVs was performed by analyzing the fluorescence emissions (λ_{ex} = 488 nm; 485 nm < λ_{em} < 565 nm) of cells after 0, 4, 24 h and 72 h of nanoparticle treatment. Statistical analysis was performed using ANOVA, followed by a HSD test.

Assessment of cell viability/apoptosis and metabolic activity

The apoptotic effects of the LMNV-assisted magnetothermal stimulation were investigated using U-87 MG cells after 4 days of treatment with chronic AMF, using flow cytometry. Samples treated with free TMZ, LMNVs, TMZ-LMNVs, and untreated samples were exposed to AMF (20 mT, 750 kHz) for 2 h per day for 4 days. After 72 h the cells were trypsinized and incubated with annexin V-FITC/PI (Thermo Fisher) for cell death assessment by flow cytometry. Before flow cytometry the cells were stained using the following procedure: cells were washed with Dulbecco's phosphate-buffered saline solution (DPBS) without calcium and magnesium and detached using trypsin–EDTA (0.25%, 5 min at 37 °C). After a centrifugation step (10 min at 3000 rpm), cells were stained with 2.5 μM of annexin V-FITC and 1 μg ml^{-1} of propidium iodide (PI) in annexin V binding buffer (1×) for 15 min at 37 °C protected from light. Cells stained with annexin V-FITC/PI were evaluated using a Beckman Coulter CytoFLEX. The percentages of viable and apoptotic populations were analyzed using the CytoFLEX software and subsequently reported on histograms. Untreated cells were used as controls.

Cell metabolism before and after the chronic magnetothermal stimulation was assessed using the WST-1 assay (Sigma-Aldrich) following a standard protocol described previously.[13] Briefly, cells at pre-determined time points were incubated with the WST-1 reagent (1 : 10 dilution) for 50 minutes at 37 °C and 5% CO_2, and then the supernatant absorbance at 450 nm was measured using a PerkinElmer Victor X3 UV-Vis spectrophotometer. The measured absorbance values were normalized and expressed as % with respect to the controls.

Annexin V-FITC fluorescence emission distributions were statistically compared by the Kruskal–Wallis test followed by the Nemenyi–Damico–Wolfe–Dunn *post-hoc* test; WST-1 data were analysed using ANOVA followed by the HSD test.

Immunofluorescence staining against p53 and Ki-67 markers

Immunofluorescence staining against the p53 tumor suppressor and the Ki-67 proliferation markers was performed after 4 days of chronic magnetothermal stimulation, similarly to a previously described study.[47] Briefly, after fixing cultures with 4% paraformaldehyde (PFA) in PBS (4 °C, 25 min), cell membranes were permeabilized with 0.1% Triton X-100 (Sigma-Aldrich) in PBS (room temperature, 25 min), and a subsequent blocking step with 10% goat serum in PBS (room temperature, 1 h) was carried out. Cultures were then incubated with a primary mouse monoclonal anti-p53 antibody (1 : 200 dilution, Abcam) or with a primary rabbit IgG anti-Ki-67 antibody (1 : 150 dilution, Millipore) in 10% goat serum (37 °C, 45 min), washed 5 times, and finally incubated with a staining solution composed of a TRITC-conjugated secondary anti-rabbit antibody (1 : 200; Millipore) or a FITC-conjugated secondary anti-mouse antibody (1 : 75; Millipore), and Hoechst 33342 (1 μg ml^{-1}, Invitrogen) for nucleus counterstaining.

After washing the cultures 3 times with PBS, imaging was performed using a CLSM system (C2s system, Nikon) as described above. Analysis of Ki-67^{+} nuclei was carried out with the NIS-Elements software (Nikon) by thresholding and selecting the Hoechst and Ki-67 signals by pixel intensity. Statistical analysis of the collected data was performed with ANOVA, followed by the HSD test.

BBB model characterization and LMNV crossing studies

The BBB model was obtained by culturing bEnd.3 cells (ATCC® CRL-2299™), a well-characterized immortalized mouse BEC line, at high confluence (seeding density = 8×10^4 cells per cm^2) for 5 days on porous inserts of Transwell® (Corning; average pore diameter of 3 μm) by using the same cell medium adopted for culturing the U-87 MG cells. The developed endothelial layer completely covered the porous scaffold, separating the luminal chamber (on the top) from the abluminal compartment (on the bottom).

Before performing the LMNV crossing tests, the BBB was characterized in terms of TEER (assessed with a Millipore Millicell ERS-2 Volt-Ohmmeter) and permeability to FITC-dextran (Sigma; molecular weight 4 kDa). Specifically, 100 μl of a phenol red-free medium containing 50 μg ml^{-1} of FITC-dextran were added to the luminal compartments of the BBB or of the inserts without cells (as controls); the abluminal compartments were filled with 600 μl of a phenol red-free medium. The fluorescence emission of the medium in the abluminal compartment was measured with a PerkinElmer Victor X3 spectrofluorometer (λ_{ex} = 488 nm; λ_{em} = 520 nm) at different time points (30 min, 60 min, 4 h, 24 h and 48 h). The values of fluorescence emission were converted and expressed in terms of FITC-dextran concentrations using a calibration curve, and statistically analyzed using ANOVA followed by a HSD test.

The expression of the ZO-1 marker of thigh junctions was finally verified by immunofluorescence analysis following treatment with a rabbit IgG primary antibody against ZO-1 (Invitrogen; 1 : 100 dilution in PBS supplemented with 10% goat serum; 3 h at room temperature) and a goat Alexa Fluor 488-IgG anti-rabbit secondary antibody (Invitrogen; 1 : 200 dilution in PBS supplemented with 10% goat serum; 2 h at room temperature), following the protocols described for Ki-67 and P53 immunostaining. CLSM was performed by using a C2s system (Nikon).

Concerning LMNV crossing tests, U-87 MG cells were cultured in the abluminal compartments and 1.3 mg ml^{-1} of DiO-stained nanovectors were incubated in the luminal chamber of the BBB model. At 4, 24 and 48 h of LMNV incubation, the fluorescence emission of the abluminal medium was measured and converted to concentration as described above for the FITC-dextran studies. Moreover, U-87 MG cells were trypsinized, centrifuged (10 min at 3000 rpm), and the pellet was resuspended in PBS for flow cytometry analysis (λ_{ex} = 488 nm; 500 nm < λ_{em} < 560 nm; CytoFLEX, Beckman Coulter). For the CLSM imaging, U-87 MG cells were fixed and treated with TRITC-conjugated phalloidin (100 μM; Millipore) and Hoechst 33342 (1 μg ml^{-1}; Invitrogen) for f-actin and nuclei staining, respectively.

Conclusions

In this work, we have synthesized and characterized lipid-based magnetic nanovectors (LMNVs) that can be used for synergic magnetic hyperthermia and chemotherapy against glioblastoma multiforme. The synthesized LMNVs presented excellent good SAR values, and were able to increase the temperature of media from 37 °C to 43 °C in approximately 10 min even when high volumes (1 ml) of the prepared magnetic fluid were used. In addition, both the LMNVs and the TMZ-LMNVs demonstrated an increase in terms of apoptotic effects on U-87 MG cells, the TMZ-LMNVs being more effective compared to the unloaded LMNVs. These lipid nanovectors presented also a good loading capacity (4.1%) with a sustained release profile which was found to be stimuli-dependent. Under physiological conditions the release of TMZ after 7 days was approximately 3.5%, while when low pH, increased H_2O_2, and magnetic hyperthermia were simultaneously applied, complete (100%) release of TMZ was observed. Cell uptake studies showed a progressive internalization of the nanomaterial that was mostly located in the cortical area of the cells, and that was associated with the intracellular side of the plasma membranes with a partial incorporation into acidic organelles (*i.e.*, lysosomes and late endosomes). Finally, chronic AFM treatments of U-87 MG cells incubated with TMZ-loaded LMNVs demonstrated great anticancer performances, both considering their strong apoptotic and anti-proliferative activity, resulting in an impressive reduction of cancer cell population after 4 days of chronic

stimulation (2 h per day). The strongest anticancer effects were observed by the application of the magnetothermal stimulation in the presence of the drug-loaded LMNVs, resulting into enhanced therapeutic effects with respect to samples treated just with hyperthermia or only with the drug.

The ability of the LMNVs to overcome the BBB limitation was preliminarily studied using an *in vitro* BBB model, and the results showed that after 24 h, almost 40% of the LMNVs are able to pass and to be thereafter internalized by the glioblastoma cells.

Future studies will be devoted to the functionalization of the proposed LMNVs in order to enhance their crossing through the blood–brain barrier and to facilitate their GBM delivery by exploiting dual targeting approaches. Finally, the anticancer efficiency of this multifunctional nanosystem will be tested on *in vivo* GBM models.

Conflicts of interest

There are no conflicts to declare.

Acknowledgements

This work has received funding from the European Research Council (ERC) under the European Union's Horizon 2020 research and innovation program (grant agreement no. 709613, SLaMM).

References

1 S. K. Carlsson, S. P. Brothers and C. Wahlestedt, *EMBO Mol. Med.*, 2014, **6**, 1359–1370.
2 A. Bhowmik, R. Khan and M. K. Ghosh, *BioMed Res. Int.*, 2015, **2015**, 320941.
3 G. Iacob and E. B. Dinca, *J. Med. Life*, 2009, **2**, 386–393.
4 K. Maier-Hauff, F. Ulrich, D. Nestler, H. Niehoff, P. Wust, B. Thiesen, H. Orawa, V. Budach and A. Jordan, *J. Neuro-Oncol.*, 2011, **103**, 317–324.
5 R. A. Revia and M. Zhang, *Mater. Today*, 2016, **19**, 157–168.
6 R. K. Oberoi, K. E. Parrish, T. T. Sio, R. K. Mittapalli, W. F. Elmquist and J. N. Sarkaria, *Neuro-Oncology*, 2016, **18**, 27–36.
7 G. Minniti, R. Muni, G. Lanzetta, P. Marchetti and R. M. Enrici, *Anticancer Res.*, 2009, **29**, 5171–5184.
8 C. Tapeinos, E. K. Efthimiadou, N. Boukos and G. Kordas, *Colloids Surf., B*, 2016, **148**, 95–103.
9 C. Tapeinos, A. Larranaga, J. R. Sarasua and A. Pandit, *Nanomedicine*, 2017, 2397–2405.
10 G. G. Genchi, A. Marino, C. Tapeinos and G. Ciofani, *Front. Bioeng. Biotechnol.*, 2017, **5**, 80.
11 A. Grillone, E. R. Riva, A. Mondini, C. Forte, L. Calucci, C. Innocenti, C. de Julian Fernandez, V. Cappello, M. Gemmi, S. Moscato, F. Ronca, R. Sacco, V. Mattoli and G. Ciofani, *Adv. Healthcare Mater.*, 2015, **4**, 1681–1690.
12 C. Tapeinos, M. Battaglini, M. Prato, G. La Rosa, A. Scarpellini and G. Ciofani, *ACS Omega*, 2018, **3**, 8952–8962.
13 A. Marino, S. Arai, Y. Hou, A. Degl'Innocenti, V. Cappello, B. Mazzolai, Y. T. Chang, V. Mattoli, M. Suzuki and G. Ciofani, *ACS Nano*, 2017, **11**, 2494–2508.
14 C. Tapeinos, M. Battaglini and G. Ciofani, *J. Controlled Release*, 2017, **264**, 306–332.
15 M. Munoz de Escalona, E. Saez-Fernandez, J. C. Prados, C. Melguizo and J. L. Arias, *Int. J. Pharm.*, 2016, **504**, 11–19.
16 H. Ming-Huang, L. Chung-Yu and S. Yu-Chuan, *Magnetic solid lipid nanoparticles as mediators for controlled hyperthermia*, Sanya, China, 2008.
17 A. A. Allam, M. E. Sadat, S. J. Potter, D. B. Mast, D. F. Mohamed, F. S. Habib and G. M. Pauletti, *Nanoscale Res. Lett.*, 2013, **8**, 426.
18 C. Tapeinos, in *Smart Nanoparticles for Biomedicine*, ed. G. Ciofani, Elsevier Inc., 2018, pp. 131–142.
19 T. M. Goppert and R. H. Muller, *J. Drug Targeting*, 2005, **13**, 179–187.
20 J. Kreuter, D. Shamenkov, V. Petrov, P. Ramge, K. Cychutek, C. Koch-Brandt and R. Alyautdin, *J. Drug Targeting*, 2002, **10**, 317–325.
21 T. Yamashita and P. Hayes, *Appl. Surf. Sci.*, 2008, **254**, 2441–2449.
22 T. L. Moore, L. Rodriguez-Lorenzo, V. Hirsch, S. Balog, D. Urban, C. Jud, B. Rothen-Rutishauser, M. Lattuada and A. Petri-Fink, *Chem. Soc. Rev.*, 2015, **44**, 6287–6305.
23 V. Forest and J. Pourchez, *Mater. Sci. Eng., C*, 2017, **70**, 889–896.
24 I. Lynch and K. A. Dawson, *Nano Today*, 2008, **3**, 40–47.
25 S. Bedanta and W. Kleemann, *J. Phys. D: Appl. Phys.*, 2009, **42**, 013001.
26 I. Prigogine and S. A. Rice, *Advances in Chemical Physics*, 1997.
27 M. Knobel, W. C. Nunes, L. M. Socolovsky, E. De Biasi, J. M. Vargas and J. C. Denardin, *J. Nanosci. Nanotechnol.*, 2008, **8**, 2836–2857.
28 K. Nadeem, H. Krenn, T. Traussnig, R. Wurschum, D. V. Szabo and I. Letofsky-Papst, *J. Magn. Magn. Mater.*, 2011, **323**, 1998–2004.
29 P. Hugounenq, M. Levy, D. Alloyeau, L. Lartigue, E. Dubois, V. Cabuil, C. Ricolleau, S. Roux, C. Wilhelm, F. Gazeau and R. Bazzi, *J. Phys. Chem. C*, 2012, **116**, 15702–15712.
30 E. L. Verde, G. T. Landi, J. A. Gomes, M. H. Sousa and A. F. Bakuzis, *J. Appl. Phys.*, 2012, **111**, 123902.
31 G. T. Landi, *Phys. Rev. B: Condens. Matter Mater. Phys.*, 2014, **89**, 014403.
32 M. Campanini, R. Ciprian, E. Bedogni, A. Mega, V. Chiesi, F. Casoli, C. de Julian Fernandez, E. Rotunno, F. Rossi, A. Secchi, F. Bigi, G. Salviati, C. Magen, V. Grillo and F. Albertini, *Nanoscale*, 2015, **7**, 7717–7725.
33 C. Blanco-Andujar, D. Ortega, P. Southern, Q. A. Pankhurst and N. T. Thanh, *Nanoscale*, 2015, **7**, 1768–1775.
34 C. A. Quinto, P. Mohindra, S. Tong and G. Bao, *Nanoscale*, 2015, **7**, 12728–12736.

35 P. Clerc, P. Jeanjean, N. Hallali, M. Gougeon, B. Pipy, J. Carrey, D. Fourmy and V. Gigoux, *J. Controlled Release*, 2018, **270**, 120–134.
36 C. Sanchez, D. El Hajj Diab, V. Connord, P. Clerc, E. Meunier, B. Pipy, B. Payre, R. P. Tan, M. Gougeon, J. Carrey, V. Gigoux and D. Fourmy, *ACS Nano*, 2014, **8**, 1350–1363.
37 M. Domenech, I. Marrero-Berrios, M. Torres-Lugo and C. Rinaldi, *ACS Nano*, 2013, **7**, 5091–5101.
38 M. Creixell, A. C. Bohorquez, M. Torres-Lugo and C. Rinaldi, *ACS Nano*, 2011, **5**, 7124–7129.
39 C. Y. Zhuang, N. Li, M. Wang, X. N. Zhang, W. S. Pan, J. J. Peng, Y. S. Pan and X. Tang, *Int. J. Pharm.*, 2010, **394**, 179–185.
40 G. Chen-yu, Y. Chun-fen, L. Qi-lu, T. Qi, X. Yan-wei, L. Wei-na and Z. Guang-xi, *Int. J. Pharm.*, 2012, **430**, 292–298.
41 O. Szasz, G. Andocs, T. Kondo, M. U. Rehman, E. Papp, T. Vancsik and T. Krenacs, *J. Clin. Oncol.*, 2015, **33**, e22176–e22176.
42 K. E. Burns and J. B. Delehanty, *Ther. Delivery*, 2017, **8**, 235–237.
43 S. Y. Lee, *Genes Dis.*, 2016, **3**, 198–210.
44 M. Rehman, A. Madni, D. Shi, A. Ihsan, N. Tahir, K. R. Chang, I. Javed and T. J. Webster, *Nanoscale*, 2017, **9**, 15434–15440.
45 A. Khan, S. S. Imam, M. Aqil, Y. Sultana, A. Ali and K. Khan, *Beni-Suef Univ. J. Appl. Sci.*, 2016, **5**, 402–408.
46 A. Marino, M. Battaglini, D. De Pasquale, A. Degl'Innocenti and G. Ciofani, *Sci. Rep.*, 2018, **8**, 6257.
47 A. Marino, C. Filippeschi, G. G. Genchi, V. Mattoli, B. Mazzolai and G. Ciofani, *Acta Biomater.*, 2014, **10**, 4304–4313.